Chapter VI

The Nucleation Nursery

> The Lord took Abram [Abraham] outside and said, "Look up at the sky and count the stars—if indeed you can count them." Then he said to him, "So shall your offspring be."
>
> The Book of Genesis, Chapter 15, Verses 3–5, New International Version

> Understand, then, that those who have faith are children of Abraham.
>
> St. Paul's Letter to the Galatians, Chapter 3, Verse 7, New International Version

Thanks to Dr. Huikuan Chao for developing the string method model of bubble nucleation and teaching me how to use it. Thanks to Prof. Richard Flagan for suggesting the idea of comparing the bubble statistics to Poisson statistics to evaluate whether the nucleation observed is uncorrelated.

Bubbles do not often nucleate homogeneously. As discussed in Chapter I, bubbles prefer to nucleate with the assistance of a surface or contamination through heterogeneous nucleation or grow from an existing microbubble when they have the chance to do so. A bubble that nucleates homogeneously has therefore avoided an easier pathway through a site that is seen until the mother phase can nucleate all bubbles at once through the unseen thermal fluctuations. At this moment, all bubbles emerge as children of the same mother phase and grow together in the same nursery of its mother. We cannot know the location or time of the nucleation of any

individual bubble, but through faith in the unseen workings of the mother phase, everywhere bubbles will gain life.

In this Chapter, these are the fingerprints by which we will distinguish homogeneous bubble nucleation from heterogeneous: randomness and rapid onset. They are also the features of homogeneous bubble nucleation that make it difficult to measure (as discussed in Section III.1). Homogeneous bubble nucleation results from thermal fluctuations, so nucleation events are independent of each other and uncorrelated. Such events are described by the Poisson statistical distribution. In Section VI.1, we show that the time interval between observations of bubble nucleation indeed follows behavior expected of Poisson distributed events, at least in the experiments for which sufficient bubbles were observed for meaningful statistics. Additionally, because homogeneous bubble nucleation occurs homogeneously, all nucleation "sites" can nucleate bubbles simultaneously. Given the high sensitivity of the nucleation barrier to the degree of supersaturation (see discussion of classical nucleation theory in Section I.4), the onset of an observable rate of bubble nucleation will be rapid in a system with an increasing supersaturation like the present apparatus (see pressure profile sketched in Figure III.2). We estimate the nucleation rate as a function of the supersaturation (estimated by the pressure) in Section VI.2 and show that the rate increases rapidly within a short window of the degree of supersaturation (pressure in the capillary).

We chose these fingerprints to distinguish homogeneous bubble nucleation because drawing the distinction from the observation of a single bubble is often not possible. In some cases, the distinction is obvious: a cluster of bubbles emanating from an oddly shaped particle is likely the result of heterogeneous nucleation from the cavities along with the contaminant particle. In most cases, however, an individual bubble that nucleates by homogeneous nucleation and a bubble that nucleates by heterogeneous nucleation appear the same. This similarity is even true in the apparatus described in Chapter III because, while the inner stream of polyol and CO_2 does not come into contact with the interior walls of the apparatus, it may contain sub-micron particles or metastable microbubbles not detectable with optical microscopy [1]. Bubbles can nucleate heterogeneously on sub-micron particles or emerge from microbubbles and leave no optically detectable trace of a particle, which often limits the experimentalist's ability to declare that a bubble nucleated by homogeneous nucleation (see Section 1.6 of [2]).

While we cannot ever prove that the bubbles observed nucleated homoge-

neously without more careful elmination of sub-micron nucleation sites, we can at least identify the bubbles whose behavior is consistent with homogeneous nucleation (which we will define as having the two fingerprints mentioned in the introduction: stochasticity and rapid onset with supersaturation) and estimate their rate of nucleation. We can then more meaningfully compare our experimental measurements to theoretical models of homogeneous bubble nucleation. Most models describe homogeneous bubble nucleation because heterogeneous nucleation is dependent on the microscopic geometry of the nucleating particles, which is often not known. In Section VI.3, we describe a model for estimating the nucleation energy barrier by applying the string method to the density functional theory described in Section II.4. We then show that this model of the nucleation energy barrier can be fit to the nucleation rates estimated from experiments in Section VI.4, while noting the limitations of modeling the nucleation rates with classical nucleation theory. Finally, we offer recommendations for the extension of this work in Section VI.5.

VI.1 Time between Nucleation Events Described by Poisson Statistics

The Poisson statistical distribution describes the occurrence of discrete, independent, and identically distributed probabilistic events. A classic example of such an event is the emission of a radioactive particle from an isotope undergoing radioactive decay because the emission of one particle has essentially no effect on the emission of the next. Under the proper circumstances, homogeneous bubble nucleation is also described by Poisson statistics. Given a collection of identical samples of fluid held at a fixed supersaturation, the nucleation of a bubble inside a sample is described by the Poisson distribution. This concept was used by Dr. Adam Olsen to estimate the nucleation rate of polyethylene oxide crystals in aqueous droplets at different activities of water [3]. In that case, the nucleation of crystals could take up to an hour and individual droplets could be held under fixed conditions and observed by Mie scattering inside a droplet levitation chamber. In the present apparatus (Chapter III), samples of polyol and CO_2 in the inner stream rapidly change in supersaturation as they flow down the observation capillary, so Olsen's experimental approach cannot be exactly replicated. Nevertheless, when the flow is stable, the degree of supersaturation at a particular location along the observation capillary remains constant. If we assume that the inner stream fluid is uniform, the segment of fluid observed at one moment has the same likelihood of nucleating as the segment of fluid observed at any other moment. Therefore, while the fluid particles themselves are not identical, the properties of the fluid under observation

are identical with respect to the factors relevant to bubble nucleation, so we treat the fluid within the field of view as the same sample over time.

One key property of Poisson-distributed events is that their occurrences are governed by first-order kinetics [4]. Consequently, given a collection of N_0 samples, the number of samples that has not yet nucleated decays exponentially with time $N = N_0 e^{-kt}$, where the decay constant k gives the frequency of nucleation events (see discussion on pp. 2-24 to 2-25 of [3]). In the present experiment, we do not continuously observe a sample of fluid, but although the fluid in the section of the flow observed is constantly replaced, its replacement is essentially identical throughout the experiment until a bubble appears. By assuming that the fluid in the section of the flow observed does not significantly change in properties, in particular, supersaturation of dissolved CO_2, we can treat the fluid in that section as a single "sample" in between bubbles.

The fluid within the field of view is not identical when it contains a bubble. A bubble reduces the volume of fluid in which another bubble can nucleate both by its volume and by the volume of fluid surrounding it from which it has collected its CO_2. Consequently, the fluid within the field of view is only identical in between observations of bubbles. Therefore, we treat the fluid within the field of view as if it is a single sample of fluid held at fixed supersaturation, neglecting the small variation in the pressure and, thus, the supersaturation along the field of view. From this perspective, the fluid within the field of view between bubble observations is like one of the droplets in Olsen's work, and the time between bubble observations is a reasonable estimate for the time that a single fluid sample would take to nucleate a bubble. However, bubbles are sometimes observed long after nucleation (see Chapter VIII). In these cases, we cannot consider the observable segment of fluid to have nucleated a bubble, but because it has been disturbed by the passing of a bubble, we also cannot consider it to be an identical sample. Consequently, we only consider segments of fluid observed between two bubbles that nucleated within the field of view, ignoring the rest of the experiment for this analysis.

Because we only consider segments of fluid between bubbles that nucleate within the field of view, the number of measured incubation times is few for most experiments. Nevertheless, in a couple of experiments, enough incubation times could be measured to compare N to exponential decay. Measurements from two such experiments are shown in Figure VI.1. In these experiments, the inner stream was composed of PPG 2700 g/mol (see Table II.1) saturated with CO_2 at 72 bar (7.2

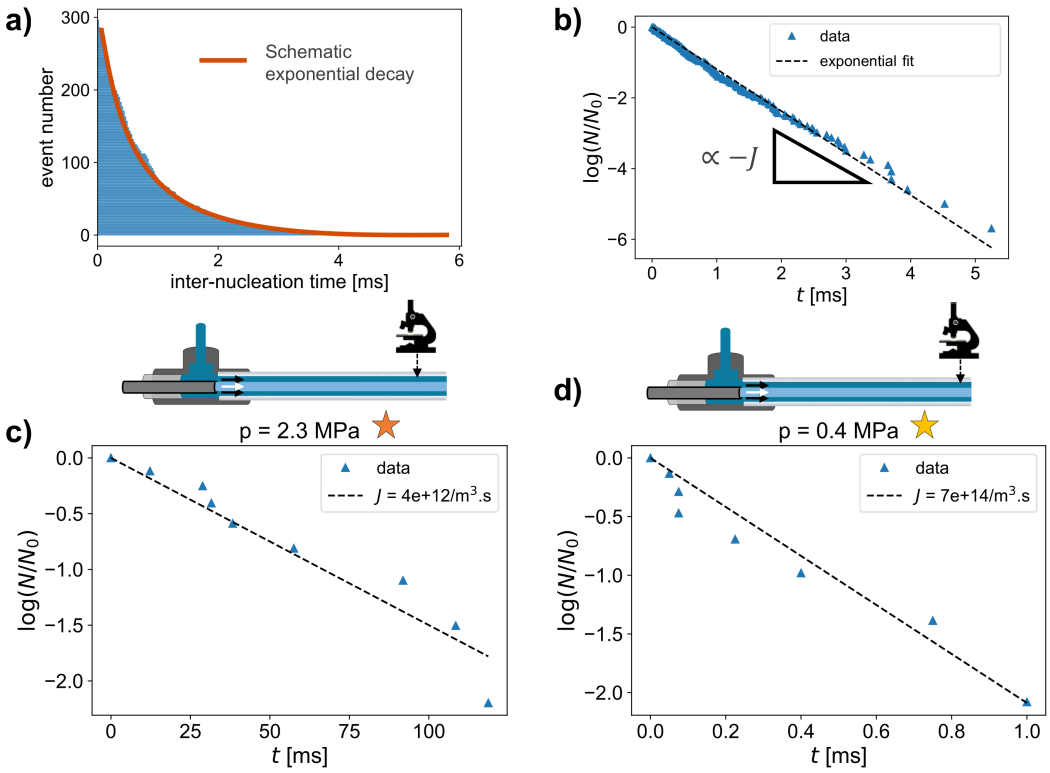

Figure VI.1: a) Time between consecutively observed nucleation events ("inter-nucleation time") plotted in decreasing order with schematic of an exponential decay fit. Data taken at 77 mm while flowing a 5:1 mixture of PPG 2700 g/mol polyol with cyclopentane saturated with CO_2 at 7.2 MPa with an inlet pressure of 13.4 MPa (too few bubbles without cyclopentane). b) The natural logarithm of the fraction of not-yet-decayed samples $\log(N/N_0)$ is fit to a straight line (dashed black) passing through the origin ($N(t=0) \equiv N_0$), indicating exponential decay. The slope of the fit is proportional to the nucleation rate J. c) and d) Data were taken in an identical experiment in the absence of cyclopentane. The location of each measurement is depicted schematically above each plot. From exponential fits (dashed lines), the nucleation rate J is calculated (see legend for values). The measurements in (c) were taken at 83 mm along the observation capillary (2.3 MPa) with an inlet pressure of 13.4 MPa; the estimated nucleation rate will be represented by an orange star. The measurements in (d) were taken at 95 mm along the observation capillary (0.4 MPa) with an inlet pressure of 8.4 MPa; the estimated nucleation rate will be represented with a yellow star.

MPa, 1045 psi), and flowed at 50 μL/min inside a sheath of 1k5f polyol, within a quartz capillary of 300 μm inner diameter. For the data shown in Figure VI.1a,c, the outer stream was flowed at 320 μL/min, resulting in an inlet pressure of 134 bar (13.4 MPa, 1945 psi). For the data shown in Figure VI.1b,d, the outer stream was flowed at 210 μL/min, resulting in an inlet pressure of 84 bar (8.4 MPa, 1220 psi).

In the top row, the incubation time of each sample (horizontal axis) is plotted to give a visual depiction of the stochasticity. The number of samples that have not nucleated N is computed from the data in the top row by drawing a horizontal line at each time point on the vertical axis and counting how many bars it passes through. In the bottom row, the natural logarithm of the fraction of the number of samples that have not nucleated $\log(N/N_0)$ is plotted as a function of time. While fewer measurements were available in this experiment to draw a definitive conclusion about the quality of the fit, at both pressures considered, 2.3 MPa (Fig. VI.1a,c) and 0.4 MPa (Fig. VI.1b,d), the exponential decay fits reasonably well. Note that the incubation times differ by two orders of magnitude between the two pressures due to the significantly higher nucleation rate at the lower pressure. That the number of samples that have not nucleated decays exponentially suggests that the bubble nucleation observed is a Poisson process and thus is likely homogeneous. For stronger evidence of this conclusion, see Figure VII.2.

The decay of N is not always fit well by an exponential function. In some cases, $\log(N/N_0)$ contains clusters of nucleation times that follow different decay rates. We suspect that the different clusters correspond to variations in the flow conditions or supersaturation. Such variations may arise due to variations in the volume occupied by bubbles at the end of the observation capillary or other flow fluctuations. We have not explored the factors that correlate with these clusters, however. In other cases, a few fluid samples have a significantly longer incubation time than the others, such that most incubation times follow a single decay rate with a few outliers. Given that we only record ~ 10 measurements per experiment, we suspect that these variations would be lessened by taking more measurements, as observed in Chapter VII where nucleation rates are higher.

As mentioned, the decay rate k is equal to the frequency of bubble nucleation in the sample volume. Therefore, the nucleation rate per volume J can be computed by dividing the frequency by the volume of the fluid sample k/V, where $V = \pi R_i^2 L_{FOV}$, with R_i as the inner stream radius and L_{FOV} as the length of the field of view within which we can detect bubbles during an experiment. This estimation method likely underestimates the nucleation rate because the cross-sectional area of fluid that is actually at the reported degree of supersaturation is smaller than the cross-sectional area of the inner stream due to depletion of CO_2 by diffusion into the outer stream (as discussed in Chapter V). Because we have not developed and validated an accurate estimate for this depletion of CO_2, we assume no depletion

for consistency. The reported nucleation rates J should thus not be interpreted as precise estimates of the true nucleation rate, but rather as rough estimates for comparison within the context of the present work. The nucleation rates estimated by this method are reported in the legends of Figure VI.1c,d. These nucleation rates are compared to the string method model in Figure VI.6. The ability to be described by the model gives further support for our hypothesis that the bubble nucleation is homogeneous and described by Poisson statistics.

VI.2 Estimation of Nucleation Rate vs. Pressure Indicates Rapid Onset of Bubble Nucleation

The other property we use to demonstrate that bubble nucleation is homogeneous is the rapid onset with increasing supersaturation. Heterogeneous bubble nucleation can occur at much lower degrees of supersaturation and is limited in rate by the rate at which bubbles leave the nucleation site. Homogeneous bubble nucleation occurs rapidly and throughout the bulk and is extremely sensitive to the degree of supersaturation. The sensitivity of homogeneous bubble nucleation to the supersaturation was demonstrated in the measurements of bubble nucleation in superheated liquids by Avedisian [5] (see Figure 2, in particular).

To demonstrate the onset of bubble nucleation, we count the number of nucleation events per time at points along the observation capillary, each corresponding to a different degree of supersaturation. As discussed in Section V.3, by fitting a model of bubble growth to a sequence of measurements of the radius of a bubble over time, we can estimate the nucleation time by extrapolating the model backward in time to the critical radius of nucleation. This time t_{nuc} can be converted into a distance along the observation capillary d_{nuc} by multiplying by the centerline flow speed v_{max} (since bubbles rarely nucleate away from the center of the inner stream). This distance can be converted to an estimate for the fluid pressure $p \approx [(L - d_{nuc})/L]p_{in}$ for capillary length L and inlet pressure p_{in}.

Because nucleation events can be rare, we count the number of nucleation events within a segment of the inner stream of length dL. The size of dL is chosen such that it is larger than the uncertainty in the capillary position (about 500 μm) but smaller than the distance over which the pressure varies significantly ($p/(\mathrm{d}p/\mathrm{d}z)$, which depends on the local fluid pressure p). In general, we bin in segments of $\mathrm{d}L = 500$ μm, which corresponds to a volume of $V = \pi R_i^2 \mathrm{d}L$ for an inner stream width of R_i. Inside each bin, we count the number of bubble nucleation events over

the course of a video recording (or series of recordings) that lasts a length of time t. During the recording, bubbles may be observed that are larger than the width of the inner stream and have elongated (see Chapter VIII). Because we have only shown that our model for bubble growth is accurate for spherical bubbles, we cannot estimate the nucleation time for these elongated bubbles. Instead, we exclude these bubbles from the count of nucleation events. We show the number of nucleation events in each such bin in Figure VI.2a. The data were taken from the same set of experiments used to produce Figure VI.1a,c.

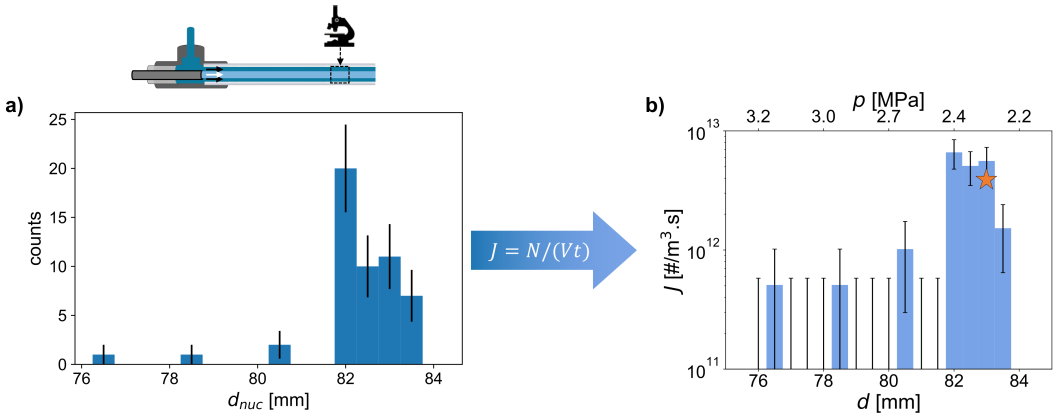

Figure VI.2: a) A histogram of the observed bubbles estimated to nucleate within the field of view of the microscope from video recordings taken at several locations along the observation capillary. Error bars represent one standard deviation of Poisson noise. Data were collected from the same experiment as Figure VI.1a,c. Location of the measurements is depicted schematically in the diagram of the microfluidic channel. b) By assuming that the number of nucleation events observed in a segment of the observation capillary is the number of observed nucleation events N in a volume V over a time t, the nucleation rate is calculated $J = N/(Vt)$ and plotted as a function of distance along the observation capillary (bottom axis) and estimated fluid pressure (top axis). Error bars are Poisson noise except in the case where no bubbles were observed (see text for explanation). The orange star represents the nucleation rate estimated by the exponential fit in Figure VI.1c.

Having shown that the nucleation events follow Poisson statistics in the previous Section, we plot error bars representing one standard deviation of the Poisson noise (proportional to the square root of the number of counts). From the counts alone, the rapid increase in bubble nucleation rate at 82 mm along the observation capillary is apparent. Nevertheless, different segments of the observation capillary may be observed for different amounts of time, so the relevant comparison is the nucleation rate. The nucleation rate is calculated by dividing the number of counts, which we assume is the expected number of counts $\langle N \rangle$, by the volume of the fluid

segment V and the time of recording t to get $J = \langle N \rangle / (Vt)$. The resulting nucleation rate is shown in Figure VI.2b. Note that the apparent decrease in the peak at 82 mm relative to the other values when converting from counts in (a) to nucleation rate in (b) is due to the longer time for which this location happened to have been observed.

While the Poisson noise offers a reasonable estimate of the uncertainty in the number of counts, it is zero for cases where no bubbles were observed. Nevertheless, a Poisson process may present no counts in an experiment even if it has an expected number of counts $\langle N \rangle > 1$. Given an expected number of counts $\langle N \rangle$ for a Poisson process, the probability of observing no counts is $e^{-\langle N \rangle}$. As a simple, first-order approximation of the uncertainty in a measurement of no counts, we assumed that a measurement of no counts is most likely an indication that the expected value was less than 1.15. We chose the cutoff of 1.15 because the probability of observing no counts given an expected value of 1.15 is $e^{-1.15} \approx 0.32$, which is the likelihood that a measurement of a Gaussian process is beyond one standard deviation from the mean. Therefore, the height of the error bars for measurements of zero counts in Figure VI.2b is the nucleation rate corresponding to the observation of 1.15 counts.

From Figure VI.2, we see that the nucleation rate rapidly increases with distance along the capillary d at $d = 82$ mm. For $d < 82$ mm, zero or one bubble nucleation events were observed during the experiment, while for $d = 82$ mm, 20 nucleation events were observed, corresponding to an increase in the nucleation rate of at least an order of magnitude over 500 μm of capillary or less than 0.1 MPa. While the increase may appear to be small on a log scale, an order of magnitude is a significant increase for such a small change in the supersaturation. This rapid rise also looks less rapid due to the apparent decrease in the nucleation rate for $d >$ 82 mm. The nucleation rate appears to decrease because the inner stream becomes increasingly filled with elongated bubbles, which are not included in the count of bubble nucleation events. More measurements are needed to reduce the uncertainty enough to probe the possibility of a sharper increase in the nucleation rate.

In Figure VI.2b, an orange star is plotted at $p = 2.3$ MPa to show the prediction of the bubble nucleation rate by the exponential decay method shown in Figure VI.1c. The predicted rate is slightly below the lower bound of the error bar. Given that nucleation rates are notoriously imprecisely measured to their exponential dependence on the system properties, we consider this agreement reasonable between the two methods. Nevertheless, we note that the estimation of nucleation rate by counting nucleation events likely underestimates the true nucleation rate

due to the exclusion of elongated bubbles, leading to an underestimate of $\langle N \rangle$, and not accounting for the depletion of CO_2 along the edges of the inner stream, leading to an overestimate of V. Therefore, we do not comment on the possibility of inconsistencies between the methods.

In this Chapter, we used the asymptotic square-root model to model the bubble growth due to the greater efficiency and simplicity with little loss in accuracy, as discussed in Section V.4. In that Section, we showed in Figure V.8 that the error in the nucleation location d_{nuc} introduced by using the square-root fit instead of the modified Epstein–Plesset model is less than 100 μm, with one outlier out of 104 having an error of 1.2 mm. To demonstrate that this error is negligible for our analysis of bubble nucleation rates, we plot the nucleation rate estimated using each model in Figure VI.3. The conditions are identical to those used to produce Figure VI.1b,d. The estimated nucleation rate is identical for every segment except the four marked with a star above. In each of these four cases, the discrepancy is within the uncertainty. This Figure demonstrates another advantage of the square-root model inside the red dashed box. At these values of p and laboratory temperature (T = 22 °C), the bubble may reach the condensation pressure of CO_2 (6 MPa [6]) as a result of the Laplace pressure during computations. Near the phase change, the model becomes stuck in an infinite loop trying to correct for the resulting errors and no estimate for the nucleation time is found. With the square-root model, the properties of CO_2 are all lumped into the effective diffusivity, so the nucleation time can be estimated at these higher pressures. The accuracy cannot be evaluated relative to the modified Epstein–Plesset model in this regime, however.

In the preceding Sections, we demonstrated that we can identify bubbles that nucleate stochastically according to Poisson statistics (Section VI.1) and suddenly upon small changes in the supersaturation (Section VI.2). As described in the introduction to this Chapter, these two properties are unique to homogeneous bubble nucleation and are not expected for heterogeneous bubble nucleation. Showing that the bubbles observed have these properties is not sufficient to prove that the bubbles nucleated homogeneously. Jones *et al.* suggest that significantly higher supersaturation ratios (order 100 or greater) are necessary for homogeneous nucleation of bubbles from a supersaturated solution. They instead propose that bubbles that nucleate at lower supersaturation ratios, such as those considered in this Chapter, emerged from metastable microbubbles temporarily stabilized by trace surfactants in the solution at sizes smaller than the spatial resolution [1]. While we cannot

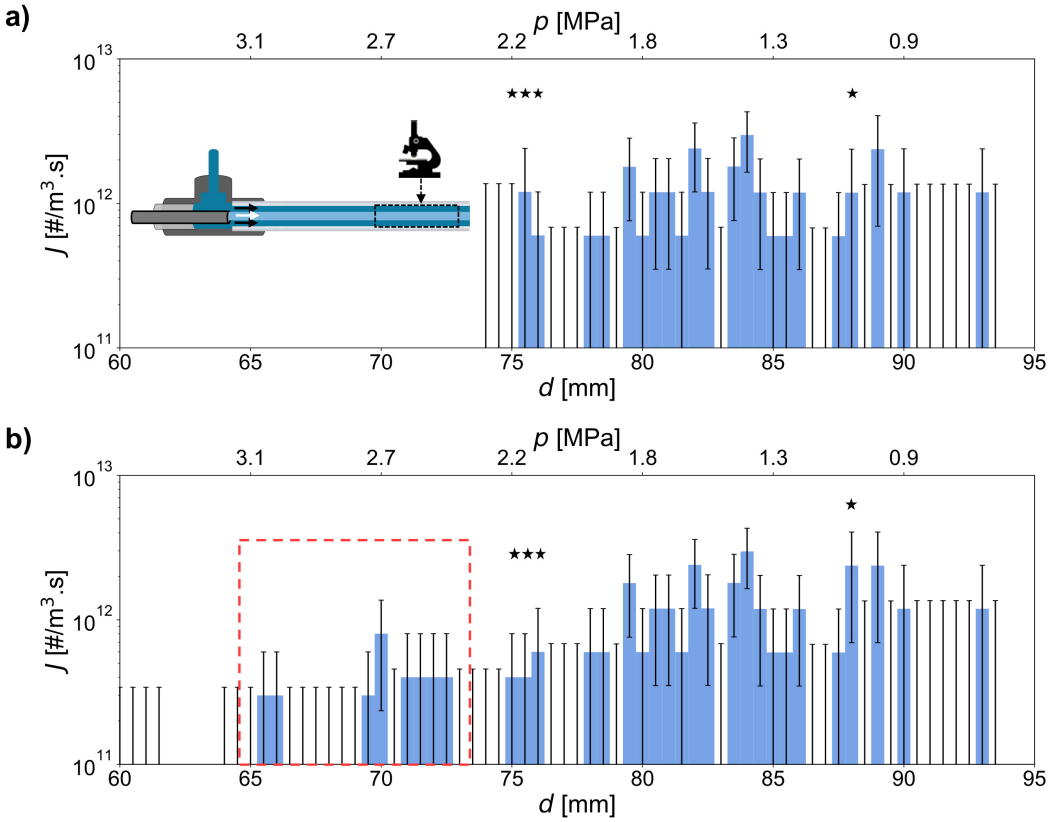

Figure VI.3: a) Nucleation rate J estimated as a function of distance along the observation capillary d (bottom axis) and estimated fluid pressure p (top axis) based on the prediction of the nucleation time from fitting the modified Epstein–Plesset model (see Section V.3). Error bars indicate Poisson noise except if no bubbles were observed (see main text for discussion). The location of the measurements is shown schematically with the diagram of the microfluidic channel. b) Same as (a), but the nucleation time is estimated from fitting the asymptotic square-root model (see Section V.4). This model permits the estimation of the nucleation rate at higher pressures (red dashed box). The four locations with different estimates for the nucleation rate between the models are marked with stars; all are within the statistical uncertainty.

completely rule out the possibility that the bubbles observed emerged from microbubbles or other sub-micron particles due to the limited spatial resolution of our optical microscope, we find that the behavior of the bubbles we observe to emerge from a sub-micron size is consistent with homogeneous bubble nucleation. Thus, we believe that they can be meaningfully compared to models of homogeneous bubble nucleation.

VI.3 Model of Bubble Nucleation Energy Barrier by Applying the String Method to a Density Functional Theory

Due to the limitations of classical nucleation theory, such as assuming an infinitesimal interface with constant interfacial tension (see discussion in Section I.4), we developed our own model of bubble nucleation. We wanted a platform that could incorporate the system-specific measurements of the mother phase provided by G-ADSA (Chapter II). Having demonstrated in Section II.4 that our density functional theory (DFT) could predict the interfacial tension between polyol-rich and CO_2-rich phases reasonably accurately, we built our model on this DFT. The string method [7] can find the minimum free energy pathway through the free energy landscape defined by the DFT, as demonstrated by Xu *et al.* [8]. A schematic of this process is shown in Figure VI.4a,b. Figure VI.4a shows the physical process of a bubble expanding from state *A* to state *B* to state *C* and, finally to state *D*. In Figure VI.4b, the same expansion is mapped along a two-dimensional projection of the free energy heatmap, with lines indicating system states with the same free energy. The initial guess for the nucleation pathway (straight black line with black circles directly from *A* to *D*) is pulled "taut" along the free energy landscape, shifting in the direction of the white left-pointing arrow until the minimum free energy pathway is found (pink line with pink circles tracing through each state). Based on the work of Xu *et al.*, collaborator Dr. Huikuan Chao applied the string method to the DFT he created for modeling the interfacial tension of the polyol–CO_2 mother phase to predict the nucleation energy barrier at different points along the observation capillary.

The output of the string method model is the density profile at each point along the minimum free energy path to nucleation. Using the DFT, the free energy of each density profile can be computed and plotted as a function of the volume of the bubble, where the surface of the bubble is usually estimated by the Gibbs dividing surface. An example of such a plot is shown in Figure VI.4c. The conditions were chosen to match those of the experiment analyzed to estimate the nucleation rates in the previous Section: PPG 2700 g/mol saturated with CO_2 at 7 MPa (70 bar, 1015 psi) and 24 °C. The free energy follows the qualitative behavior expected from the classical nucleation theory of a single nucleation barrier (marked by a star) followed by a steady decrease in the free energy. The string method assumes a quasistatic process that can partially equilibrate at each location along the string. In reality, equilibrium is only achieved at the nucleation barrier where the free energy reaches a saddle point, but the model is nevertheless valid if nucleation is slow enough

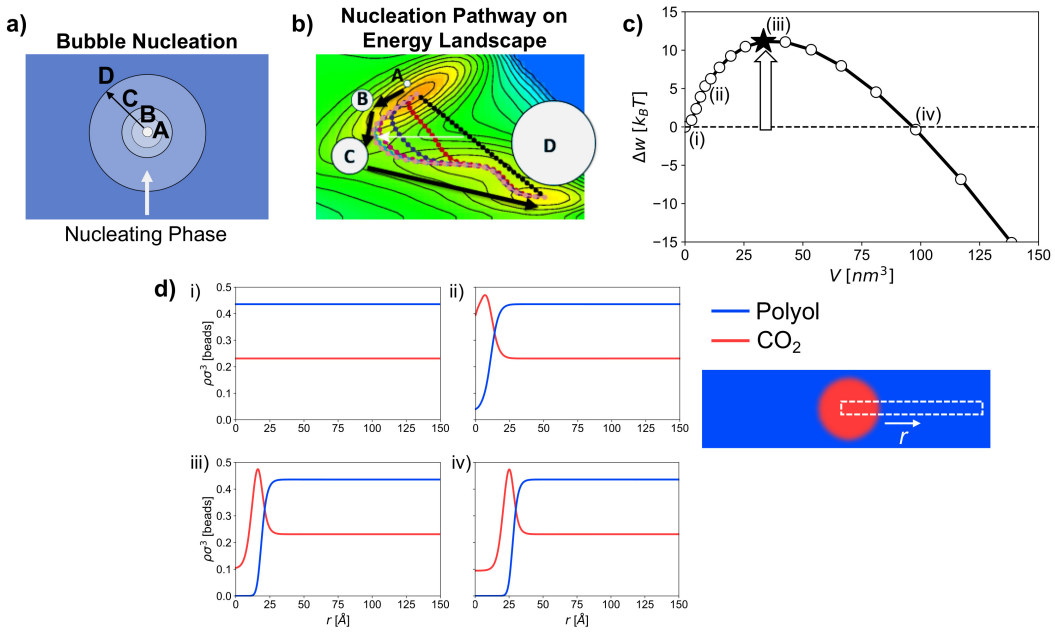

Figure VI.4: a) Schematic of bubble nucleation (light-colored circles) in a supersaturated mother phase (blue background) passing through states A, B, C, and D. b) Heatmap representing a free energy landscape for the different states passed through during nucleation (for schematic purposes only—not related to the present work). A pathway is guessed between the start (A) and end (D) states (black line with black circles). The string method then pulls the string connecting them "taut" (follow left-pointing white arrow) to find the minimum free energy path (pink line with pink circles). Adapted from Alberto Giacomello *et al.* *PNAS* 2016 113(3):E262 Copyright 2016 National Academy of Sciences. c) Prediction by the string method of the free energy along the string tracing the minimum free energy path for bubble nucleation. The conditions are: PPG 2700 g/mol polyol saturated with CO_2 at 7 MPa and 24 °C quenched to 0.1 MPa. The peak of the free energy (black star) is the nucleation energy barrier (height of white upward arrow). The indices (i)–(iv) indicate the points corresponding to the density profiles in (d). d) Density profiles from the DFT on which the string method is based of polyol (blue lines) and CO_2 (red lines) plotted in reduced units (number of beads of each compound per volume equal to the cube of the CO_2 bead size, which is 2.79 Åas given in Table II.2) as a function of radius r from the bubble center (in Angstroms). The free energy of each density profile (i)–(iv) is marked in c). The region between the bubble center and the mother phase plotted in (d) is shown schematically in the lower right with the radial direction r indicated.

that the state space can be explored before each nucleation event (see discussion in Section I.4). For more details on the formulation of the string method, refer to the presentation by Wang *et al.* [9].

While there is no evidence that the density profiles predicted by the DFT

along the path found by the string method are realized in physical systems, they provide insight into the nucleation process. Four density profiles from different points along the nucleation pathway are shown in Figure VI.4d, which are labeled (i)-(iv) with their size and free energy indicated by the same label in panel (c). In this case, the nucleation process begins from a uniform mother phase (i). To nucleate a bubble, CO_2 must be collected while expelling polyol, which costs free energy (ii). At the nucleation energy barrier, the bubble has grown to its largest size without achieving a bulk density inside. The high free energy cost is mostly driven by the large concentration gradients. Once the nucleation barrier is overcome, the bubble achieves a bulk density at its core (iv). Because the bulk phase inside the bubble is thermodynamically favorable (otherwise nucleation would not occur), the free energy cost decreases and the bubble continues to grow. Beyond this point, the predictions of the string method are not physically meaningful because they neglect diffusion limitations, convection and flow, and other macroscopic behaviors.

Because the string method is based on DFT, and the DFT is based on PC-SAFT (see Section II.4), the predictions of bubble nucleation by the string method depend on the selection of parameters for the PC-SAFT model. As discussed in Section II.4, an infinite set of PC-SAFT parameters can model the CO_2 solubility and interfacial tension measured with G-ADSA, but none can accurately model the specific volume. Rather, we found one set of parameters that accurately models the qualitative behavior of the specific volume (increases with pressure) and is similar to those predicted by the group contribution method [10]. Another set of parameters more accurately models the specific volume quantitatively (smaller discrepancy from the measurements) but predicts the opposite qualitative behavior (predicts that specific volume decreases with pressure instead of increasing). The nucleation energy barrier predicted by the string method with each of these sets of parameters is shown in Figure VI.5.

The conditions are the same as those used to generate the string method predictions shown in Figure VI.4c,d. The nucleation barrier (marked with a star) was calculated at four ambient pressures, each corresponding to a different point along the observation capillary: 4.0 MPa, 2.0 MPa, 1.0 MPa, and 0.1 MPa (outlet pressure) and plotted on the right. The prediction for the parameters that achieved a more *quantitative* fit of the specific volume (parameters listed in caption of Figure VI.5) is shown on the top; on the bottom is the prediction for the parameters that achieved a more *qualitative* fit (parameters listed in Table II.2). While these parameters lead to

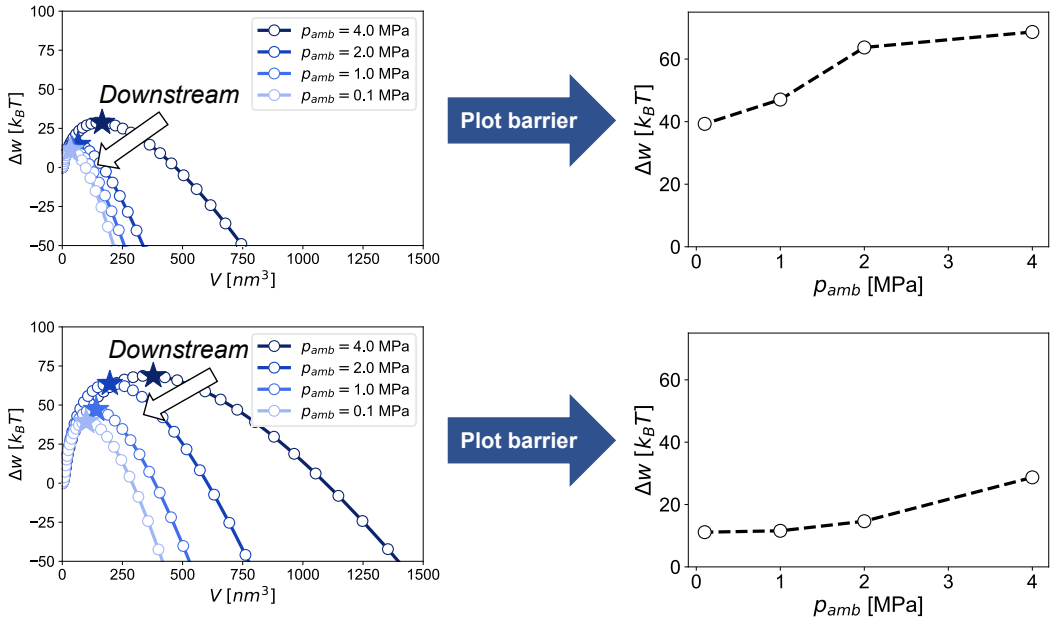

Figure VI.5: Left) Free energy Δw in units of thermal energy as a function of the bubble volume along nucleation pathways predicted by the string method for PPG 2700 g/mol polyol saturated with CO_2 at 7 MPa at 24 °C and quenched to p_{amb} = 4.0 MPa, 2.0 MPa, 1.0 MPa, and 0.1 MPa (in order of increasing lightness of blue), which corresponds to points further downstream along the observation capillary (marked by white arrow). Right) The nucleation energy barrier (marked by a star) is plotted as a function of the quench pressure p_{amb}. The model used for the top uses the PC-SAFT parameters listed in Table II.2. The model used for the bottom uses the PC-SAFT parameters that yield a better quantitative fit of the specific volume (see Figure II.2): σ = 3.17 Åand ϵ = 253 k_B.

models that predict the same CO_2 solubility and interfacial tension, as well as specific volumes within 15% of each other, they caused differences in the prediction of the nucleation barrier by the string method of 20–40 k_BT. Given that the nucleation rate depends on the negative exponent of the nucleation energy barrier scaled by k_BT, these discrepancies correspond to multiplicative differences of 10^8–10^{17} in the nucleation rate.

Because of the extreme sensitivity of the string method's prediction of the nucleation rate on the PC-SAFT parameters, the value of the string method for quantitative predictions is limited without a more rigorous and precise method for estimating the PC-SAFT parameters. While the string method provides helpful qualitative insights into the nucleation pathway by estimating the density profiles along the way, the uncertainty in the nucleation energy barrier is likely too high to be useful. Furthermore, the string method does not provide an estimate of the

coefficient J_0 needed to estimate the nucleation rate $J = J_0 e^{-\Delta W / k_B T}$. The value of J_0 may vary by several orders of magnitude depending on whether nucleation is limited more by diffusion, interfacial tension, or viscosity [11], none of which is accounted for in the string method. Despite these limitations of the application of the string method, we explore the possibility of modeling the measured nucleation rates with the string method in the following Section.

VI.4 String Method Model Can Be Fit to Measured Nucleation Rate While Classical Nucleation Theory Cannot Be

Despite the extreme sensitivity of the string method predictions of the nucleation barrier to the PC-SAFT parameters used in the model, we attempt to use its predictions to model the data from Sections VI.1 and VI.2. Given that the PC-SAFT parameters that achieved a qualitative fit of specific volume (see Table II.2) led to reasonable nucleation barriers near 10 $k_B T$ (bottom right of Figure VI.5), we select that parameter set for our model. Because the string method does not treat the nucleation coefficient J_0, we treat it as a fitting parameter to the nucleation rates reported in Figure VI.2. We find that the value $J_0 = 10^{20}$ /m^3.s yields a reasonable model for the data, as shown in Figure VI.6, with the experimental measurements shown in panel (a) and the predictions of the fitted string method model in panel (b). While we cannot comment on why such a value yields a reasonable agreement, especially given the likelihood that the estimates of the measured nucleation rate are lower than the actual rate, the model qualitatively captures the observed behavior. In the experiment, an increase in the nucleation rate by a factor of 10 was observed from 2.5 MPa to 2.4 MPa. The model shows an increase in the nucleation rate by a factor of 10 from 10^{12} to 10^{13} / m^3.s from 2.6 MPa to 2.2 MPa (see inset). While the model predicts a steeper decrease in the nucleation rate at higher pressures, the uncertainty in the measurements is too large to determine if the nucleation rate decreased as rapidly in the experimental system.

We also compared the measured nucleation rate estimated using the fit to Poisson statistics from Section VI.1. The estimated nucleation rate J from Figure VI.1c for a pressure of 2.3 MPa is plotted with an orange star and that from Figure VI.1d for a pressure of 0.4 MPa is plotted with a yellow star. Surprisingly, both values are close to the model predictions. While the string method model is not robust to parameter selection, the model resulting from this particular set of parameters captures the measurements of nucleation rate available.

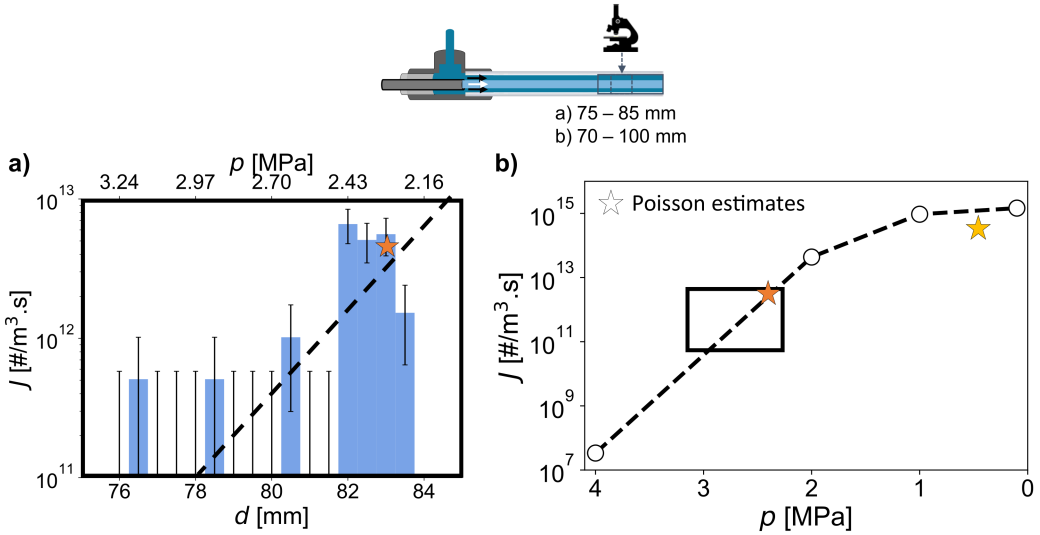

Figure VI.6: a) Same plot of estimated nucleation rate from experiments as a function of degree of supersaturation along the observation capillary as in Figure VI.2b, repeated for convenience, now with the fitted model from the string method plotted as a black dashed line. b) Model of bubble nucleation rate J using the string method model used to generate the top plots in Figure VI.5. Black box indicates the axis limits of (a) for more direct comparison. The orange star indicates the nucleation rate estimated from Figure VI.1c and the yellow star indicates the nucleation rate estimated from Figure VI.1d.

Classical Nucleation Theory

While we focused on the string method model, we want to address the limitations of classical nucleation theory (CNT) that persuaded us not to pursue it as a model of bubble nucleation. CNT assumes that (1) the interface between the bubble and the mother phase is infinitesimal and (2) the interfacial tension remains constant during nucleation. However, the present thesis has shown that (1) the interface between the bubble and the mother phase has a significant accumulation of CO_2 (see Figure II.S14) and (2) the interfacial tension varies significantly during bubble nucleation (see purple line in Figure V.7). Therefore, we do not expect CNT to model bubble nucleation in the present system accurately, although it is sometimes used to model bubble nucleation in polymer foams in the literature [12].

To give quantitative evidence of the poor suitability of CNT for modeling bubble nucleation in this system, we estimate the nucleation energy barrier predicted by CNT at the outlet of the observation capillary under the same conditions as used for the string method model in this Section. Based on the more convenient form of the nucleation energy barrier in equation I.6, the nucleation energy barrier

$$\frac{\Delta G^*}{k_B T} = \frac{16\pi}{3} \frac{\gamma^3}{(\Delta p)^2 k_B T}$$

where $\Delta p = p_{sat} - p$ with p_{sat} representing the pressure at which the gas was originally saturated into the fluid.

At the outlet of the observation capillary, the pressure is atmospheric pressure, 0.1 MPa. At this pressure, the interfacial tension between the polyol-rich and CO_2-rich phases is $\gamma \approx 30$ mN/m (see Figure II.3a), assuming equilibrium is rapidly attained. In our example, the saturation pressure was $p_{sat} = 7$ MPa. This formulation of CNT thus estimates the nucleation barrier to be

$$\begin{aligned} \Delta G^* &\approx \frac{16\pi}{3} \frac{(0.03 \text{ N/m})^3}{(7 \times 10^6 \text{ Pa} - 10^5 \text{ Pa})^2 (10^{-23} \text{ J/K})(300 \text{ K})} \\ &\sim 1000 \end{aligned}$$

A nucleation energy barrier of $1000\, k_B T$ is unphysically low and suggests that nucleation would be impossible, despite our observations that nucleation happens readily at higher pressures. While CNT could be adapted to achieve more physically relevant results, such as by adjusting the interfacial tension based on DFT predictions [8], we focused on the string method model due to the greater physical insight it provided.

In the present Section, we showed that some observations of bubble nucleation in a mixture of polyol supersaturated with CO_2 occur both stochastically and increase in nucleation rate sharply with supersaturation. We showed that the nucleation is stochastic by fitting the time between nucleation events, the "incubation time" of the inner stream, to an exponential decay, which is characteristic of the independent and identically distributed events of a Poisson process (see Figure VI.1). We showed that the nucleation rate sharply increases with supersaturation by estimating the nucleation rate at various locations along the observation capillary, which corresponds to various fluid pressures and thus degrees of supersaturation. The rate of bubble nucleation increased by at least an order of magnitude over a change in the pressure of about 0.1 MPa (see Figure VI.2). These two properties

provided support for our hypothesis that most of the bubble nucleation included in the analysis is consistent with homogeneous nucleation rather than heterogeneous. Therefore, we compared these estimates of bubble nucleation rate to a theoretical model that applied the string method to the density functional theory discussed in Chapter II. While the model was extremely sensitive to certain parameters (see Figure VI.5), it could reasonably model the estimated nucleation rates with the introduction of a fitted coefficient (see Figure VI.6). Classical nucleation theory, however, predicted extremely high nucleation barriers that would have suggested bubble nucleation were impossible under the conditions considered.

VI.5 Recommendations for Future Work

The most natural next step for future work on this topic is to take more measurements of bubble nucleation with the current method and perform the analysis presented on a larger dataset. By taking more measurements, the number of bubbles observed at each location increases, decreasing the relative size of the Poisson noise. By reducing uncertainty in the estimated nucleation rate, we can more precisely test our hypothesis that the bubble nucleation rate increases sharply with supersaturation, as is typical for homogeneous bubble nucleation. Taking more measurements can also expand the parameter space explored and reveal trends. For example, by varying the saturation pressure of CO_2, the assumption by classical nucleation theory that only the difference between the saturation pressure and the fluid pressure determines the bubble nucleation energy barrier (assuming a fixed interfacial tension; see equation I.6) could be tested. Additionally, by varying the flow speed, the role of depletion of CO_2 could be tested.

Another flow property that could be varied would the width of the inner stream. Because the number of nucleation events is proportional to the volume of the supersaturated fluid, for a given volume of fluid, only a limited range of nucleation rates will result in enough bubble nucleation events to be detected but not so many that they significantly deplete the available CO_2 and space to nucleate in. By increasing that volume, smaller nucleation rates can produce a detectable quantity of nucleation events; by decreasing that volume, larger nucleation rates will nucleate few enough bubbles to be measured. The width of the inner stream affects many other properties, however. The wider the inner stream, the faster the flow. Flow that is too fast will cause motion blur, reducing spatial resolution, and increase the distance traveled between frame captures, reducing time resolution. A wider inner stream will also lose a smaller fraction of CO_2 through diffusion into the

outer stream. In fact, in experiments, the number of observed bubbles dramatically increased with the increase in the inner stream flow rate despite a negligible change in the inlet pressure. If the inner stream is too narrow, it will lose its CO_2 more quickly both due to the smaller quantity of CO_2 contained and the longer residence time due to the slower flow speed. Within these limits, however, the variation of the inner stream radius can increase the range of bubble nucleation rates that can be probed with this method.

The conclusions of this Chapter could also be probed more rigorously through more careful and thoughtful analysis. In the present analysis, the entire inner stream is considered to be uniformly supersaturated based on the assumption that no CO_2 has been lost to diffusion and no bubbles are occupying space in the stream. In reality, a significant fraction of the inner stream has typically lost enough CO_2 that bubble nucleation is significantly suppressed. Additionally, not only can bubble nucleation not occur when a bubble is occupying a region of the inner stream, but it may also be suppressed in the wake of CO_2-depleted fluid it leaves behind (see discussion of the wake in Chapter VIII for more details). Accounting for the reduction in the volume of supersaturated fluid that can nucleate bubbles caused by these phenomena may significantly increase the estimated nucleation rate.

Another important part of the analysis is the accurate estimation of the fluid pressure. Because of the small dimensions of the capillary and the impossibility of machining ports into it, the pressure along the observation capillary cannot be directly measured with a pressure transducer. The introduction of mechanophores or compressible microbubbles could someday provide an estimate of the local pressure, assuming that they can be tailored to tolerate pressures over 10 MPa and adjust to the local pressure on the scale of milliseconds. Nevertheless, the pressure could also be estimated through indirect means. For example, given that we can estimate the inlet pressure reasonably accurately, we assume that deviations from a linear pressure drop are the result of bubbles in the inner stream, over which the pressure drop is negligible (see Figure 8 of Khandekar *et al.* [13]). By measuring the fraction of the time that the inner stream is occupied by a bubble along its length, one could estimate the reduction in the pressure drop across that portion of fluid by integrating this fraction from the outlet of the observation capillary.

While we showed reasonable agreement between a string method model and estimated nucleation rates from experiments, the high sensitivity of the string method model to the PC-SAFT parameters limits its utility without precise estima-

tion of these parameters. A more precise estimate of these parameters would thus increase the utility of the string method, although it may require the incorporation of association interactions (see discussion in Section II.5).

More precise comparison with the string method predictions of the nucleation barrier could also be achieved by estimating the nucleation barrier from measurements of the nucleation rate at different temperatures but fixed supersaturation using the second nucleation theorem, as originally presented by Ford [14] and further explained by Laaksonen and Malila [15]. The second nucleation theorem relates the derivative of the logarithm of the nucleation rate with temperature at fixed supersaturation to the nucleation energy barrier. Changing the temperature changes the degree of supersaturation, so to keep the degree of supersaturation consistent between measurements of the bubble nucleation rate taken at different temperatures, nucleation must be observed at higher pressures for higher temperatures. The pressure corresponding to the desired degree of supersaturation at a given temperature could be determined using the PC-SAFT model discussed in Section II.4. The distance along the observation capillary corresponding to that pressure could be estimated based on our assumption of a constant pressure gradient from the entrance to the exit of the observation capillary with a small correction for the reduced pressure gradient in the region near the exit of the capillary where a foam is formed.

References

1. Jones, S., Evans, G. & Galvin, K. Bubble nucleation from gas cavities a review. *Advances in Colloid and Interface Science* **80,** 27–50. ISSN: 00018686. https://linkinghub.elsevier.com/retrieve/pii/S0001868698000748 (Feb. 1999).

2. Brennen, C. E. *Cavitation and Bubble Dynamics* 1–290. ISBN: 0195094093. https://authors.library.caltech.edu/25017/5/BUBBOOK.pdf (Oxford University Press, New York, 1995).

3. Olsen, A. P. *Scanning Activity Gravimetric Analysis (SAGA) of Aqueous Polyethylene Oxide* PhD thesis (California Institute of Technology, 2006), 1–5–4.

4. Turnbull, D. Kinetics of solidification of supercooled liquid mercury droplets. *The Journal of Chemical Physics* **20,** 411–424. ISSN: 00219606 (1952).

5. Avedisian, C. T. The Homogeneous Nucleation Limits of Liquids. *Journal of Physical and Chemical Reference Data* **14,** 695–729. ISSN: 15297845 (1985).

6. NIST. *NIST Standard Reference Database Number 69* 2022. https://webbook.nist.gov/chemistry/ (2022).

7. E, W., Ren, W. & Vanden-Eijnden, E. String method for the study of rare events. *Physical Review B* **66,** 052301. ISSN: 0163-1829. https://link.aps.org/doi/10.1103/PhysRevB.66.052301 (Aug. 2002).

8. Xu, X., Cristancho, D. E., Costeux, S. & Wang, Z.-G. Bubble nucleation in polymer–CO2 mixtures. *Soft Matter* **9,** 9675. ISSN: 1744-683X. www.rsc.org/softmatter%20http://xlink.rsc.org/?DOI=c3sm51477c (2013).

9. Wang, Z.-G. *et al. Bubble Nucleation in Polymer-CO2 Mixtures* in *APS March Meeting 2020 Session S33: Physics of Foams: Fundamentals and Applications* (American Physical Society, 2020). https://absuploads.aps.org/presentation.cfm?pid=17459.

10. Tihic, A., Kontogeorgis, G. M., von Solms, N., Michelsen, M. L. & Constantinou, L. A Predictive Group-Contribution Simplified PC-SAFT Equation of State: Application to Polymer Systems. *Industrial & Engineering Chemistry Research* **47,** 5092–5101. ISSN: 0888-5885. https://pubs.acs.org/doi/10.1021/ie0710768 (Aug. 2008).

11. Blander, M. & Katz, J. L. Bubble nucleation in liquids. *AIChE Journal* **21,** 833–848. ISSN: 15475905 (1975).

12. Kim, K. I., Kang, S. L. & Kwak, H. Y. Bubble nucleation and growth in polymer solutions. *Polymer Engineering and Science* **44,** 1890–1899. ISSN: 00323888 (2004).

13. Khandekar, S., Panigrahi, P. K., Lefèvre, F. & Bonjour, J. Local Hydrodynamics of Flow in a Pulsating Heat Pipe: A Review. *Frontiers in Heat Pipes* **1.** ISSN: 2155-658X. https://www.thermalfluidscentral.org/e-journals/index.php/Heat_Pipes/article/view/103 (Nov. 2010).

14. Ford, I. J. Thermodynamic properties of critical clusters from measurements of vapour–liquid homogeneous nucleation rates. *The Journal of Chemical Physics* **105,** 8324–8332. ISSN: 0021-9606. http://aip.scitation.org/doi/10.1063/1.472687 (Nov. 1996).

15. Laaksonen, A. & Malila, J. in *Nucleation of Water: From Fundamental Science to Atmospheric and Additional Applications* 45–70 (2022).